

# EDiffSR: An Efficient Diffusion Probabilistic Model for Remote Sensing Image Super-Resolution

Yi Xiao<sup>✉</sup>, Qiangqiang Yuan<sup>✉</sup>, Member, IEEE, Kui Jiang<sup>✉</sup>, Member, IEEE,  
Jiang He<sup>✉</sup>, Graduate Student Member, IEEE, Xianyu Jin<sup>✉</sup>, and Liangpei Zhang<sup>✉</sup>, Fellow, IEEE

**Abstract**—Recently, convolutional networks have achieved remarkable development in remote sensing image (RSI) super-resolution (SR) by minimizing the regression objectives, e.g., MSE loss. However, despite achieving impressive performance, these methods often suffer from poor visual quality with oversmooth issues. Generative adversarial networks (GANs) have the potential to infer intricate details, but they are easy to collapse, resulting in undesirable artifacts. To mitigate these issues, in this article, we first introduce diffusion probabilistic model (DPM) for efficient RSI SR, dubbed efficient diffusion model for RSI SR (EDiffSR). EDiffSR is easy to train and maintains the merits of DPM in generating perceptual-pleasant images. Specifically, different from previous works using heavy UNet for noise prediction, we develop an efficient activation network (EANet) to achieve favorable noise prediction performance by simplified channel attention and simple gate operation, which dramatically reduces the computational budget. Moreover, to introduce more valuable prior knowledge into the proposed EDiffSR, a practical conditional prior enhancement module (CPEM) is developed to help extract an enriched condition. Unlike most DPM-based SR models that directly generate conditions by amplifying LR images, the proposed CPEM helps to retain more informative cues for accurate SR. Extensive experiments on four remote sensing datasets demonstrate that EDiffSR can restore visual-pleasant images on simulated and real-world RSIs, both quantitatively and qualitatively. The code of EDiffSR will be available at <https://github.com/XY-boy/EDiffSR>.

**Index Terms**—Diffusion probabilistic model (DPM), image super-resolution (SR), prior enhancement, remote sensing.

## I. INTRODUCTION

SUPER-RESOLUTION (SR) is a long-standing issue and remains an active research topic in the area of remote sensing [10]. SR aims to reconstruct a high-resolution (HR) image with rich texture details from a low-resolution (LR) image [11], [12], [13]. Currently, SR has been widely explored in remote sensing applications, including land-cover mapping [14], [15], [16], hyperspectral image fusion [17], [18],

Manuscript received 23 September 2023; revised 10 November 2023; accepted 1 December 2023. Date of publication 12 December 2023; date of current version 20 December 2023. This work was supported in part by the National Natural Science Foundation of China under Grant 42230108 and Grant 61971319. (*Corresponding author: Qiangqiang Yuan*.)

Yi Xiao, Qiangqiang Yuan, Jiang He, and Xianyu Jin are with the School of Geodesy and Geomatics, Wuhan University, Wuhan 430000, China (e-mail: xiao\_yi@whu.edu.cn; yqiang86@gmail.com; jiang\_he@whu.edu.cn; jin\_xy@whu.edu.cn).

Kui Jiang is with the School of Computer Science and Technology, Harbin Institute of Technology, Harbin 150000, China (e-mail: kuijiang\_1994@163.com).

Liangpei Zhang is with the State Key Laboratory of Information Engineering in Surveying, Mapping, and Remote Sensing, Wuhan University, Wuhan 430000, China (e-mail: zlp62@whu.edu.cn).

Digital Object Identifier 10.1109/TGRS.2023.3341437

product reconstruction [19], and vehicle tracking [20]. Due to the inherently ill-posed nature [21], [22], [23], [24], SR is challenging, because the HR counterpart may be infinite in the solution space given an LR input. In particular, for large-scale Earth observation scenarios, SR becomes more complicated owing to various degradations [25], such as atmospheric scattering and platform tremors. Therefore, developing an effective SR method to reconstruct high-quality images is indispensable and of practical importance.

Convolutional methods have shown significant success in modeling the nonlinear relationship between LR and HR images in recent years. Among them, various efforts have been made to tame the inherent ill-posedness, such as dense [26], [27] and residual networks [28], attention-based models [3], [29], and transformer architectures [4], [30]. However, the existing methods often employ regression function, e.g., mean-squared error (MSE) and mean absolute error (MAE), to minimize the pixel-level difference between super-resolved results and ground-truth images. Despite obtaining favorable peak signal-to-noise ratio (PSNR) performance, these optimal objects can lead the model to average the pixel distance, resulting in oversmooth results. To restore visually convincing details, deep generative adversarial networks (GANs) [5] have been explored. Such methods exploit the adversarial optimization between the generator and the discriminator to encourage the generator to recover realistic images. In general, GANs require carefully designed loss functions as auxiliary, e.g., perceptual loss [6] and gradient loss [7], to optimize the distance in the feature domain. Although GANs can generate rich details, they often suffer from training instability and are easy to collapse, leading to undesirable artifacts.

Recently, diffusion probabilistic models (DPMs) [31] have received increasing attention in the realm of image-to-image translation and also achieved promising performance in SR tasks [8], [32], [33], [34]. The key to DPM is the reverse diffusion process, which iteratively predicts various noises from a noisy image. In this manner, DPM can generate high-quality data distributions from random noise. Because of its principled and well-defined probabilistic diffusion process, DPM can mitigate the training instability that commonly occurs in GANs and generate more complex distributions. More recently, Saharia et al. [8] pioneered the DPM-based SR method and utilized the UNet as the denoiser to generate images by iterative refinement. To better simulate the degradation process, Luo et al. [9] proposed stochastic differential equations (SDEs) to model the diffusion process. Nevertheless, most DPM-based SR methods remain confined within the

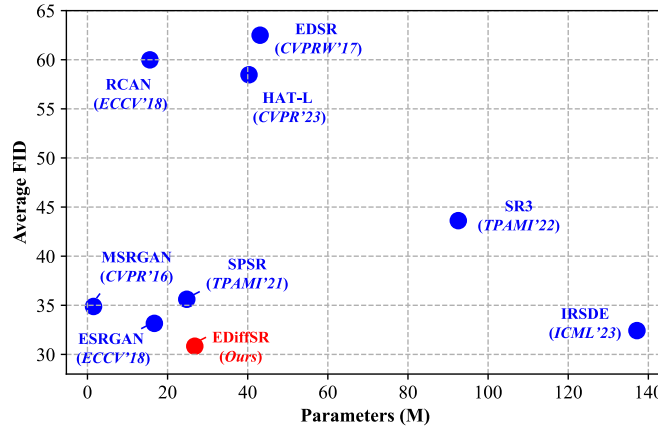


Fig. 1. Relationship between FID [1] performance and parameter of SOTA SR methods (lower FID values indicate better generative quality). EDSR [2], RCAN [3], and HAT-L [4] are regression-based models, typically generating low-quality distribution. The GAN-based approaches (MSRGAN [5], ESRGAN [6], and SPSR [7]) and DPM-based methods (SR3 [8] and IRSDE [9]) can produce high-quality images. Our EDiffSR achieves the best performance and is far more lightweight than SOTA DPM-based SR models.

paradigm of image synthesis tasks, lacking insightful design for SR tasks. Specifically, the following hold.

- 1) *Prior Knowledge in LR Image, Which Is Critical for SR Tasks, Is Rarely Explored:* Following the paradigm of image synthesis, the LR image is often directly upsampled by bicubic interpolation to serve as the condition. This preprocessing scheme lacks elaboration and can only convert partial prior knowledge into a diffusion model. As a result, it may lead to suboptimal performance.
- 2) *Vanilla UNet Consumes Massive Computational Cost and Is Less Effective in SR Tasks:* In contrast to image synthesis, which needs to predict an image from scratch, more pixels of SR are given. Thus, employing a large network for noise prediction is inefficient.

To this end, this article explores the application of DPM and devises an efficient diffusion model for RSI SR (EDiffSR). Unlike previous work that applied bicubic-upsampled LR image as the condition, we developed a novel conditional prior enhancement module (CPEM) to effectively leverage prior knowledge in LR images. It promotes the condition with more informative and plentiful input. Moreover, an efficient activation block (EAB) is devised to form our denoising network (EANet), achieving favorable denoising capability while maintaining a far more lightweight design. As illustrated in Fig. 1, our EDiffSR achieves impressive performance while with significantly fewer parameters than previous DPM-based SR approaches (e.g., SR3 [8] and IRSDE [9]). In addition, we equip our EDiffSR with the SDEs [9] to further facilitate the sampling process in the diffusion process. Extensive evaluations on four remote sensing datasets demonstrate the superiority of our EDiffSR in both perceptual quality and quantitative metrics over the state-of-the-art (SOTA) regression-based, GAN-based, and DPM-based models.

In summary, the main contributions of this study are summarized as follows.

- 1) We pioneer an efficient yet effective DPM (EDiffSR) for remote sensing image (RSI) SR. By introducing

more prior knowledge into the diffusion model with elaborate CPEM, our EDiffSR can achieve accurate SR performance.

- 2) The proposed EANet can exceed the previous SOTA methods in noise prediction while with lower computational cost. It provides a new perspective for exploring more efficient diffusion-based frameworks.

The remainder of this article is organized as follows. Section II reviews the progress of image SR and diffusion models. Section III presents some preliminary of the diffusion process. Section IV introduces the implementation details of our EDiffSR. Section V contains experiments and analysis. Section VI is the conclusion.

## II. RELATED WORK

### A. Deep Learning-Based Image SR

1) *Regression-Based Models:* Inspired by the success of SRCNN [35], numerous elaborate CNN architectures have been proposed, such as very deep [28] and wide [2] architectures, attention mechanism [3], [29], and transformer [4]. Recently, Chen et al. [4] proposed an impressive method by combining the advantage of channel attention and self-attention to activate more useful information for SR. However, most regression-based SR approaches predict the target distribution by minimizing the MSE ( $L_2$ ) or MAE ( $L_1$ ) loss. While achieving high PSNR values, the regression functions often tend to encourage the network to “average” a certain region, leading to an undesirable oversmooth issue. In contrast, our EDiffSR can benefit from the generative capability of DPM to recover more realistic distributions, improving the visual quality of SR results by a large margin.

2) *GAN-Based Models:* To promote visual pleasure, GAN-based SR approaches introduce elaborate auxiliary loss to guide the network to generate photorealistic results. For example, Ledig et al. [5] pioneered the perceptual loss that measures the featurewise distance between the restored image and the ground-truth image in VGG feature space [36]. To tame the training stability, Wang et al. [6] put forward an enhanced SRGAN (ESRGAN) with modified discriminative constraints while removing batch normalization (BN) to avoid artifacts. Sajjadi et al. [37] developed a texture loss to preserve the high-frequency textual details. Recently, Ma et al. [7] proposed a structural preserving GAN that maintains structural information by the gradient loss. Although GANs can bring impressive improvement in visual quality, they often face harsh optimization problems. Moreover, we often require laborious tricks to strike the balance between these carefully designed loss functions. Benefiting from the well-defined diffusion process, the proposed EDiffSR offers a stable and interpretable training process.

3) *Diffusion-Based Models:* Diffusion models use a fixed Markov chain to optimize the variations boundaries of the likelihood function and have recently received increasing attention due to their excellent performance on generative tasks [38]. In SR task, research on diffusion modeling is still in its infancy. Until recently, Saharia et al. [8] proposed to generate results that exceed those of the GAN with iterative refinement.

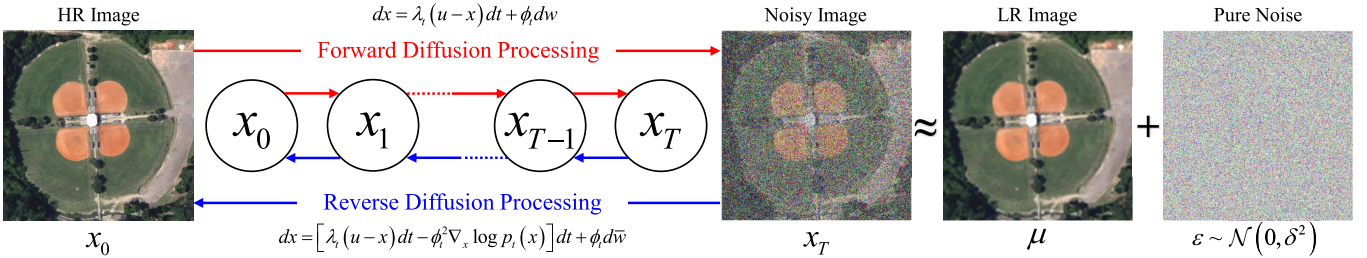


Fig. 2. Overview of the forward and reverse diffusion processes defined by mean-reverting SDEs. The forward diffusion gradually degrades the high-quality and HR image  $x_0$  to its low-quality counterpart via  $x_T = \mu + \varepsilon$ . The reverse diffusion learns to characterize the noise and reconstruct the corresponding HR image.

Li et al. [32] first introduced the residual prediction in DPM for face image SR. More recently, Xia et al. [39] exploited the transformer block to model the long-range discrepancy for effective image restoration. Luo et al. [9] proposed an averaging-equation idea to simulate the image degradation process while realizing a faster diffusion process. However, current DPM-based SR models often rely on large models for noise prediction. The high complexity of denoisers limits their practical application and leads to inefficient inference in large-scale remote sensing scenarios. In contrast, the proposed EDiffSR achieves favorable noise prediction with a far more lightweight EANet. Besides, the existing methods barely consider the prior information in images, which is crucial for SR tasks, thus resulting in suboptimal performance. The proposed EDiffSR seeks a more desirable condition by exploring informative cues from the LR images, which further boosts the SR performance.

### B. RSI Super-Resolution

Early SR methods for RSI are regression-based, aiming to achieve high PSNR performance [40], [41], [42]. In this parse, more efforts have been paid to improve the network structure, making the convolution network grasp more characteristics of RSIs, such as multiscale design [43], [44], [45], numerous attentions [46], [47], and guided SR [48]. Li et al. [49] proposed a novel dual-stage network to reconstruct more missing details in remote sensing imagery in a coarse-to-fine manner. Recently, Li et al. [50] put forward to transfer more beneficial supplementary from red-green-blue (RGB) images to remote sensing scenes. However, as PSNR tends to penalize the reconstruction of high-frequency details, these methods cannot reflect human preference well in RSI.

To recover visual-pleasant details in RSI, various GAN-based methods have been proposed. Lei et al. [51] proposed a coupled-discriminated GAN for better discrimination. Jiang et al. [52] proposed an edge-enhanced GAN by optimizing the high-frequency and low-frequency components simultaneously. Haut et al. [53] proposed to train a GAN in an unsupervised manner without the HR RSI. Recently, Tu et al. [54] incorporated the long-range modeling capability of the Swin transformer [55] into GAN, achieving favorable perceptual quality of SR results. However, these approaches often involve complex optimization functions and network structures, leading to training instability. In contrast, this article proposed an efficient solution to

recover perceptual-pleasant RSI, mitigating the training instability of GAN.

In the area of remote sensing, some researchers have applied diffusion modeling to SR tasks [33], [56]. However, they borrow too much from the paradigm in image synthesis, which uses a large UNet for noise estimation, resulting in inefficient inference in SR tasks. In addition, there is a lack of consideration of incorporating the valuable prior knowledge in diffusion to generate high-frequency details in RSIs. In this article, we demonstrate that a low-complexity network can provide a more practical and efficient scheme to deliver competitive denoising performance in SR tasks when compared with SOTA methods employing larger models, such as UNet. In addition, unlike simple bicubic upsampling, we choose to explore more prior information to generate informative conditions, thus further enhancing the diffusion model to generate realistic distributions.

## III. PRELIMINARY

### A. Forward Diffusion Process

The forward diffusion process aims to gradually transform the initial data distribution  $x_0$  to a noisy image  $x_T$  after time step  $T$ . As shown in Fig. 2, we define the ground-truth image  $I_{\text{HR}}$  as  $x_0$ . As such,  $x_T$  can approximately to the combination of the bicubic-upsampled LR image  $\mu$  and a pure Gaussian noise  $\varepsilon \sim \mathcal{N}(0, \delta^2)$ . Here,  $\delta^2$  represents the stationary variance. This article adopts the mean-reverting SDEs [9] to define the diffusion process, as it allows for an efficient sampling process. Specifically, as illustrated in Fig. 2, the forward diffusion process is depicted as follows:

$$dx = \lambda_t(u - x)dt + \phi dw \quad (1)$$

where  $w$  refers to a standard Wiener process.  $\lambda_t$  and  $\rho_t$  are two time-dependent parameters that control the speed of mean reversion and stochastic volatility, respectively. To make (1) have a closed-form solution, we set  $\phi_t^2/\lambda_t = 2\delta^2$ . As shown in Fig. 2, given an HR image  $x_0$  and  $t \in [0, T]$ , for an intermediate moment  $t$ , the corresponding state  $x_t$  can be strictly expressed by the closed-form solution of (1)

$$x_t = \mu + (x_0 - \mu)e^{-\bar{\lambda}_t} + \int_0^t \phi_z e^{-\bar{\lambda}_z} dw(z) \quad (2)$$

where  $\bar{\lambda}_t$  is equal to  $\int_0^t \lambda_z dz$ . The proof of (2) can be found at [9]. In this case,  $x_t$  follows a Gaussian probability distribution  $p_t(x)$ , expressed as follows:

$$x_t \sim p_t(x) = \mathcal{N}(x_t | m_t(x), n_t) \quad (3)$$

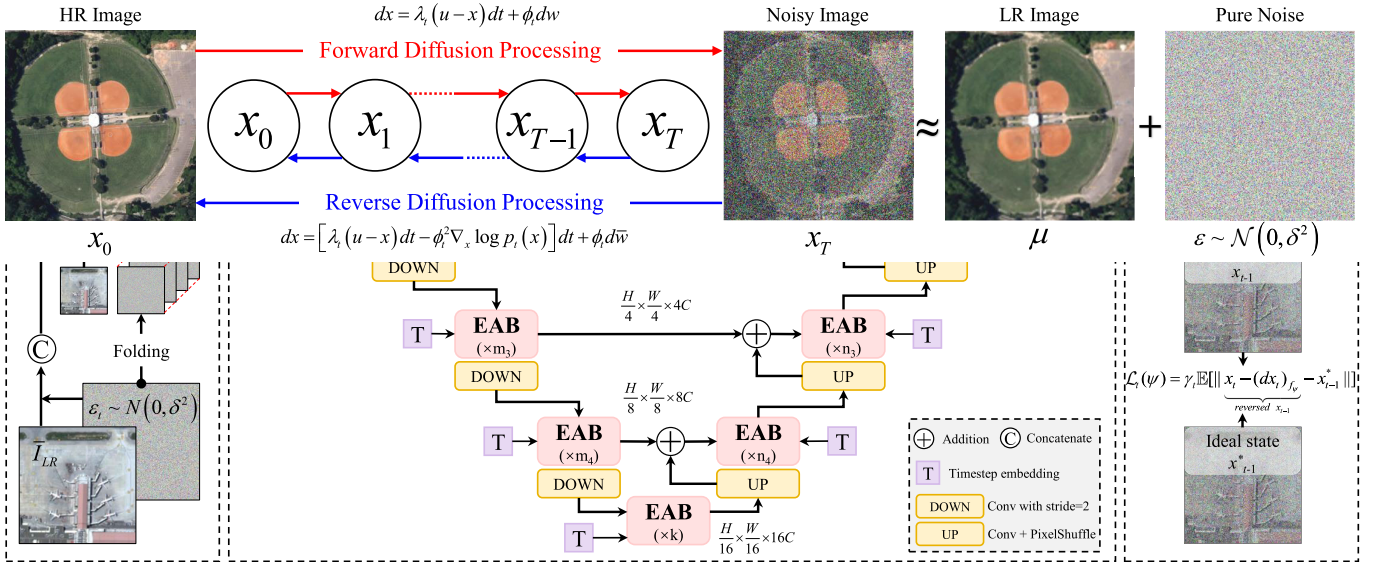


Fig. 3. Overall framework of our EDiffSR. It consists of three parts: the condition part, EANet, and the optimization part. In the condition part, CPEM is designed to explore more priors from the original LR image. EANet takes the condition as input and characterizes the noise distribution. Compared with the primary UNet, it is more efficient and effective owing to the EAB. The optimization process adopts the maximum likelihood learning for a more stable diffusion process.

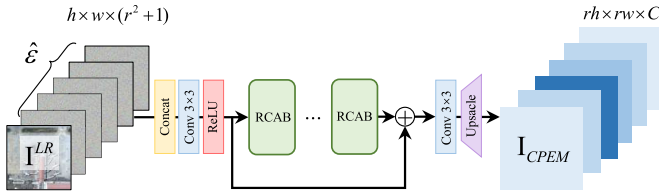


Fig. 4. Flowchart of CPEM. We adopt the RCAB to extract rich prior information.

where  $m_t(x) = \mu + (x_0 - \mu)e^{-\bar{\lambda}_t}$  and  $n_t = \delta^2(1 - e^{-2\bar{\lambda}_t})$  are the mean and variance of this Gaussian distribution, respectively. It is easy to observe that as the diffusion time  $t \rightarrow \infty$ ,  $m_t$  and  $n_t$  would converge to  $\mu$  and  $\delta^2$ , i.e., the terminal state  $x_T \approx \mu + \varepsilon$ , which aligns with the aim of the forward diffusion process.

### B. Reverse Diffusion Process

Reverse diffusion aims to recover the HR image from the terminal state  $x_T$ . We can define the reverse diffusion process by simulating the reverse-time SDE as follows:

$$dx = [\lambda_t(u - x)dt - \phi_t^2 \nabla_x \log p_t(x)]dt + \phi_t d\bar{w} \quad (4)$$

where  $\bar{w}$  denotes a reverse-time Wiener process.  $\nabla_x \log p_t(x)$  is the ground-truth score during inference stage. Note that in the training stage, the ground-truth image  $x_0$  is available; thus, we can leverage more pleasurable conditional scores during model training. In particular, it can be defined by

$$\nabla_x \log p_t(x|x_0) = -\frac{x_t - m_t(x)}{n_t}. \quad (5)$$

Furthermore, we reparameterize  $x_t$  to  $x_t = m_t(x) + \sqrt{n_t} \varepsilon_t$ , where  $\varepsilon_t$  is a standard Gaussian noise with the distribution  $\mathcal{N}(0, I)$ . The ground-truth scores can be expressed as  $-(\varepsilon_t / \sqrt{n_t})$ . Since  $m_t(x)$  and  $n_t$  are known, then we just need to estimate the noise using a noise prediction network  $f_\psi$ .

Similar to DPM [31], we compute the Euclidean distance between the predicted noise and the ground-truth noise  $\varepsilon_t$  by the following formula:

$$\mathcal{L}(\psi) = \sum_{t=0}^T \gamma_t \mathbb{E} \left[ \left\| \underbrace{f_\psi(x_t, u, v, t)}_{\text{predicted noise } \bar{\varepsilon}_t} - \varepsilon_t \right\| \right] \quad (6)$$

where  $\gamma_t$  denotes the positive weight and  $v$  refers to the original LR image.

## IV. PROPOSED METHOD

### A. Overview

Fig. 3 details the flowchart of our proposed EDiffSR. In the input part, we perform conditional prior enhancement to generate a more pleasurable condition for noise prediction. Specifically, the prior enhancement module  $f_{\text{CPEM}}$  takes the random noise  $\varepsilon_t$ , LR image  $v$ , and the corresponding bicubic-upsampled LR image  $\tilde{I}_{\text{LR}}$  as input, and then produces the enriched condition  $I_t$  by the following formula:

$$I_t = f_{\text{CPEM}}(v, \hat{\varepsilon}_t) + f_3([\mu, \varepsilon_t]) \quad (7)$$

where  $\hat{\varepsilon}_t = \text{Fold}(\varepsilon_t)$  represents that we adopt the pixel-folding operator to downsample the scale of  $\varepsilon_t$  without loss spatial information.  $f_3(\cdot)$  is a  $3 \times 3$  convolution, and  $[\cdot]$  represents channelwise concatenation. Subsequently, a conditional time-dependent network  $f_\psi$  takes the pleasurable condition and time  $t$  as input, aiming to output a pure noise

$$\bar{\varepsilon}_t = f_\psi(I_t, t). \quad (8)$$

Here, we proposed an EANet for noise prediction. Finally, we can optimize  $f_\psi$  until it converges.

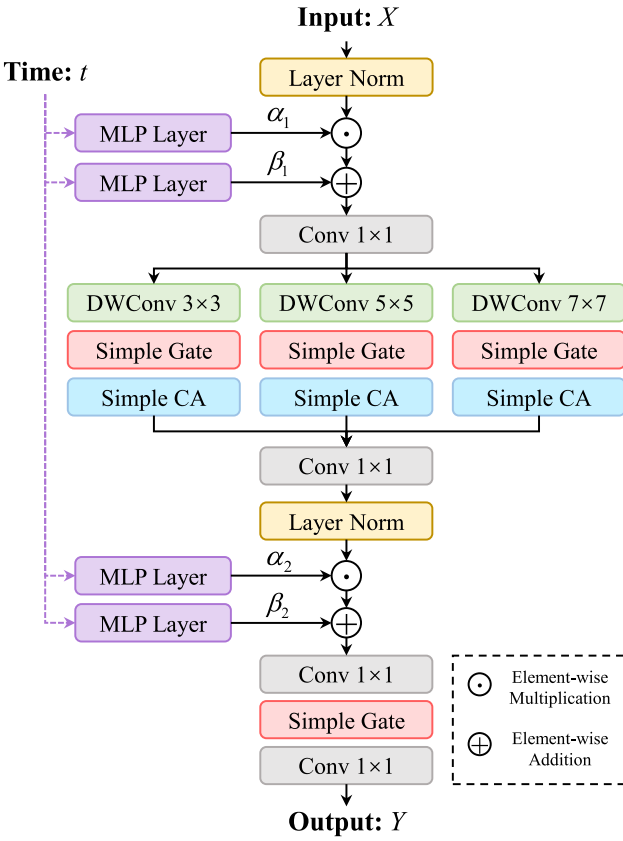


Fig. 5. Illustration of the EAB.

### B. Conditional Prior Enhancement Module

Most previous methods have typically prepared the condition input by simply upsampling the LR image using bicubic interpolation. However, for SR tasks, this scheme may lose critical structure information, resulting in suboptimal conditional inputs. In contrast, our EDiffSR proposes to generate a more informative condition by exploring additional prior knowledge from the LR image, thus enriching the condition information for better SR performance.

As shown in Fig. 4, the CPEM mainly consists of a convolution layer and ReLU activation, followed by stacked residual channel attention blocks (RCABs) [3] and an upscale layer. To unify the scale of noise and the LR image, we first convert  $\varepsilon_t$  to the noisy cube using pixel folding. Then, we concatenate and pass them through a  $3 \times 3$  convolution layer followed by ReLU activation to perform shallow feature extraction, depicted as follows:

$$I_0 = \text{ReLU}(\text{Conv}(\text{Concat}(v, \hat{\varepsilon}_t))). \quad (9)$$

Subsequently,  $n$  cascaded RCABs  $f_{\text{RCAB}}$  are used to achieve deep feature extraction and stabilize the gradient by global residual connection

$$I_{\text{deep}} = f_{\text{RCAN}}^n(I_0) + I_0. \quad (10)$$

Following that, a  $3 \times 3$  convolution and a PixelShuffle layer [57] are used to get the condition yield from CPEM:

$$I_{\text{CPEM}} = \text{PixelShuffle}(\text{Conv}(I_{\text{deep}})). \quad (11)$$

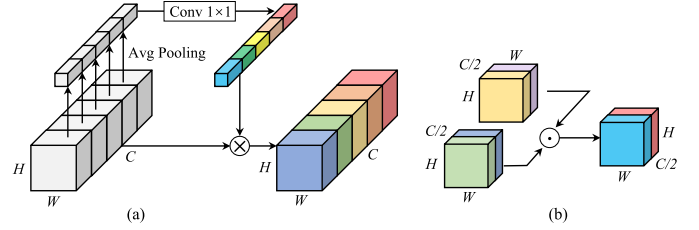


Fig. 6. Flowchart of (a) simple channel attention and (b) simple gate operation.

### C. EANet for Noise Prediction

As illustrated in Fig. 3, the key component of our EANet is the EAB. Fig. 5 displays the architecture of the EAB, showcasing its lightweight design. The EAB primarily consists of depthwise convolution (DWConv), simple channel attention, and simple gate operations. This lightweight design results in significantly lower computational complexity when compared with large UNet architectures that incorporate channel attention or self-attention mechanisms. As discussed before, in the context of SR tasks, the majority of pixels are known. Therefore, a large model running massive calculations is inefficient in SR and may lead to a suboptimal performance due to redundant inference. Our EANet offers a more practical scheme to achieve favorable denoising performance with a lightweight model.

As shown in Fig. 5, given an input  $X$  and time step  $t$ , EAB predicts an output  $Y$ . In particular,  $t$  will be projected to two flatten features  $\alpha$  and  $\beta$  by MLP layer for feature modulation

$$F = f_{1\times 1}(\alpha_1 \odot \text{Norm}(X) + \beta_1). \quad (12)$$

More precisely,  $\alpha$  functions as a scaling operation, while  $\beta$  is adopted for feature shift. In this manner, the time step  $t$  can be embedded into our EANet, making EANet aware of the current state of the diffusion process for better noise prediction. Subsequently, we use multiscale DWConv to explore the multiscale knowledge in RSI. Within each scale, we incorporate additional nonlinear representations through the use of simple channel attention and simple gate activation, as illustrated in Fig. 6. To simplify the channel attention [3], we eliminate the convolution layer and sigmoid activation. The simple gate activation is essentially an elementwise product operation applied to the feature maps. The multiscale simple activation process can be expressed as follows:

$$\begin{cases} F^3 = \text{SCA}(\text{SimpleGate}(f_{3\times 3}(F))) \\ F^5 = \text{SCA}(\text{SimpleGate}(f_{5\times 5}(F))) \\ F^7 = \text{SCA}(\text{SimpleGate}(f_{7\times 7}(F))). \end{cases} \quad (13)$$

After that, we set a  $1 \times 1$  convolution to aggregate these multiscale representations  $F' = f_{1\times 1}(\text{Concat}(F^3, F^5, F^7))$ . After layer norm, we conduct modulation with the scaling and the shifting operation

$$\bar{F} = \alpha_2 \odot \text{Norm}(F') + \beta_2. \quad (14)$$

Finally, the output  $Y$  can be obtained via the following formulation:

$$Y = f_{1\times 1}(\text{SimpleGate}(f_{1\times 1}(\bar{F}))). \quad (15)$$

Following previous works [9], [33], we form our EANet to a U-shape encoder-decoder structure. During the encoding phase, we employ a sequence of EABs and a convolution operation with a stride of 2 to progressively downsample the feature maps. In the decoding phase, multiple EABs and pixel-shuffle layers are used to upscale the features. The number of EABs in the encoder and decoder component is denoted as  $[m_1, m_2, m_3, m_4]$  and  $[n_1, n_2, n_3, n_4]$ , respectively. In addition, we introduce  $k$  EABs in the middle of the EANet.

#### D. Optimization and Inference

Although (6) can provide a straightforward solution to optimize the EANet, the diffusion model often suffers from instability in the training process. The key reason is predicting an instantaneous distribution of noise is not an easy task. Therefore, we modified the training object by using a maximum likelihood learning strategy used in [9]. To optimize EANet, specifically, we choose to minimize the Euclidean distance below

$$\mathcal{L}(\psi) = \sum_{t=0}^T \gamma_t \mathbb{E} \left[ \left\| \underbrace{x_t - (dx_t)_{f_\psi}}_{\text{reversed } x_{t-1}} - x_{t-1}^* \right\| \right] \quad (16)$$

where  $x_{t-1}^*$  is the ideal state reversed from  $x_t$ . The closed form of  $x_{t-1}^*$  can be determined by the following formula:

$$\begin{aligned} x_{t-1}^* &= \frac{1 - e^{-2\bar{\lambda}_{t-1}}}{1 - e^{-2\bar{\lambda}_t}} e^{-\bar{\lambda}'_t} (x_t - \mu) \\ &\quad + \frac{1 - e^{-2\bar{\lambda}'_t}}{1 - e^{-2\bar{\lambda}_t}} e^{-\bar{\lambda}_{t-1}} (x_0 - \mu) + \mu. \end{aligned} \quad (17)$$

The proof can be referred to [9]. In brief, we transformed the distance between the predicted noise and ground-truth noise into another domain, i.e., the distance between the ideal state and the predicted state. This scheme helps to reduce the optimization instability, as most pixels in reversed states are known.

In the inference procedure, we utilize the pretrained  $f_\psi$  to predict HR images by sampling from the random state  $x_T$  and iteratively solve the SDE with numerical solutions, such as the Euler–Maruyama method [58]. To better understand the training and inference process of our EDiffSR, we summarize these processes in two algorithms, as presented in Algorithms 1 and 2.

## V. EXPERIMENT AND DISCUSSION

#### A. Dataset

We use four public remote sensing datasets to comprehensively evaluate the effectiveness of the methods in this article, including AID [59], DOTA [60], DIOR [61], and NWPU-RESISC45 [62]. The training set in this study consists of 3000 randomly selected images from the AID dataset with an image size of  $640 \times 640$ . Specifically, we randomly select 100 images in each of the 30 categories of AID to build the training set. In addition, we have selected ten images from each category that do not overlap with the training set to form the test set, resulting in a total of 300 test images.

Furthermore, we have used a subset of images from the DOTA dataset and the DIOR dataset for testing, consisting of 700 and 1000 images, respectively. These images have a resolution of  $512 \times 512$ . As a result, our test set comprises a total of 2000 images. In our simulated experiments, we used bicubic interpolation for image degradation. NWPU-RESISC45 data were only used for real-world analysis without any simulated degradation. To save the inference cost, we randomly selected 315 images from NWPU-RESISC45 and cropped them to  $128 \times 128$ .

#### B. Implementation Details

This study focus on  $4 \times$  SR, i.e.,  $r = 4$ . In our final EDiffSR, we incorporate five RCAB in the CPEM for prior enhancement. The innerchannel number in EANet is set to  $C = 64$ . Following prior works [9], [33], the depth of the noise prediction network is set to 4. In particular, the number of EAB in each depth  $[m_1, m_2, m_3, m_4]$  and  $[n_1, n_2, n_3, n_4]$  is set to  $[14, 1, 1, 1]$  and  $[1, 1, 1, 1]$ , respectively. We include one EAB at the middle layer of EANet, i.e.,  $k = 1$ . To train our EDiffSR, we perform 500 000 iterations with a mini-batch size of 4. The initial learning rate is set to  $4 \times 10^{-5}$  and decays following a cosine schedule. We utilize the AdamW optimizer with  $\beta_1 = 0.9$  and  $\beta_2 = 0.999$ . The total step of the diffusion process is  $T = 100$ . All SR methods involved in this article were retrained from scratch on the AID training set. For a fair comparison, we did not perform any pretraining and fine-tuning processes in our EDiffSR. Our experiments are implemented on PyTorch with a 24-GB memory NVIDIA RTX 3090 GPU.

#### C. Metrics

In this article, seven metrics are used to comprehensively evaluate the performance of SR model. In the simulation experiments, where the ground-truth image is available, we utilize five full-reference metrics: Fréchet inception distance (FID) [1], learned perceptual image patch similarity (LPIPS) [63], deep image structure and texture similarity (DIST) [64], and the widely used PSNR and the structural similarity index (SSIM) [65]. These metrics help assess the distance between the generated images and the ground-truth images. Among them, FID is widely used to measure the generative quality of the generative model. It enhances the inception score (IS) [66] metric by directly measuring the feature-level distance without the need for a classifier. In real-world experiments without ground-truth images, we additionally report the results on two reference-free metrics: natural image quality evaluator (NIQE) [67] and average gradient (AG). These metrics offer insights into the perceptual quality and the high-frequency details of the generated images.

#### D. Comparison With SOTAs

We compared our EDiffSR with SOTA SR approaches, including EDSR [2], RCAN [3], HAT-L [4], MSRGAN [5], ESRGAN [6], SPSR [7], SR3 [8], and IRSDE [9]. We selected these methods, as they represent the mainstream approaches

**Algorithm 1** Training of our EDiffSR

---

**Input:** HR image  $x_0 = I_{HR}$ , LR image  $v = I_{LR}$ , upsampled LR image  $\mu = \bar{I}_{LR}$ , total step  $T$ .

**Initialization:** Random sample  $\varepsilon_t \sim \mathcal{N}(0, \delta^2)$ ,  $t \in [0, T]$ ,  $T = 100$ .

**repeat**

- 3  $I_t = f_{\text{CPEM}}(v, \hat{\varepsilon}_t) + \text{Conv}([\mu, \varepsilon_t]);$  // Enhance
- 4  $\bar{\varepsilon}_t = f_\psi(I_t, t);$  // Predict noise
- // Substitute score into (6)
- 5  $dx_t = [\lambda_t(u - x_t)dt - \phi_t^2 \frac{\bar{\varepsilon}_t}{\sqrt{n_t}}]dt + \phi_t d\bar{w};$
- 6  $\mathcal{L}(\psi) = \gamma_t \mathbb{E}[\underbrace{\|x_t - (dx_t)_{f_\psi} - x_{t-1}^*\|}_{\text{reversed } x_{t-1}}];$  // Loss
- 7  $\nabla_\psi \mathcal{L};$  // Gradient descent
- 8 **until** converged

---

**Algorithm 2** Inference of Our EDiffSR

---

**Input:** LR image  $v = I_{LR}$ , upsampled LR image  $\mu = \bar{I}_{LR}$ , total step  $T$ .

**Output:** The super-resolved image  $I_{SR}$ .

**Initialization:** Random sample  $x_T \sim \mathcal{N}(0, \delta^2)$ ,  $f_\psi$  is the pre-trained EANet, EM( $\cdot$ ) is Euler–Maruyama method,  $T = 100$ .

**for**  $t = T : 1$  **do**

- 3    $\bar{\varepsilon}_t = f_\psi(x_t, u, v, t);$  // Predict noise
- // Substitute score into (6)
- 4    $dx_t = [\lambda_t(u - x_t)dt - \phi_t^2 \frac{\bar{\varepsilon}_t}{\sqrt{n_t}}]dt + \phi_t d\bar{w};$
- 5    $x_{t-1} = x_t - \text{EM}(dx_t);$  // Reverse SDE

**end**

7  $I_{SR} = x_0;$

---

in the field, ensuring a comprehensive evaluation. Specifically, EDSR, RCAN, and HAT-L are regression-based approaches that adopt wide CNN, channel attention, and transformer architectures, respectively. Note that MSRGAN is a modified version of SRGAN, where the BN layer is removed to avoid artifacts, and it employs the same perceptual loss as ESRGAN. SPSR employs carefully designed gradient loss to preserve structural details and has demonstrated favorable performance. On the other hand, SR3 and IRSDE are SOTA diffusion-based models. We retrained these comparative approaches on the AID training set according to their official implementation settings.

1) *Quantitative Comparison:* Results of FID values on 30 categories of the AID test set are reported in Table I. In each row, we highlighted the best and the second-best FID performance. We can find, in most remote sensing scenes, our EDiffSR achieves favorable FID performance against all comparative models. However, due to the complex diversity of remote sensing scenes, achieving generalization across various scenes remains a challenging task. Specifically, EDiffSR outperforms the second-best approach (IRSDE) by an average margin of 1.63 in terms of FID. These results reveal that EDiffSR can provide robust high-quality data distribution in various remote sensing scenarios, highlighting its favorable generative capability.

In addition, we presented the average FID, LPIPS, DISTS, and NIQE values across the AID, DOTA, and DIOR test sets in Table II. We observed that our EDiffSR still achieves the best

FID performance across these test sets. It is worth highlighting that GAN-based models excel in achieving the best LPIPS results, because they usually adopt the VGG space [36] to compute the perceptual loss, which aligns with the calculation of LPIPS. In this case, our EDiffSR achieves acceptable LPIPS results and surpasses diffusion-based approaches by a large margin. For instance, compared with SR3, EDiffSR exhibits a remarkable 0.0647 improvement in terms of LPIPS. When compared with IRSDE, we achieve superior LPIPS performance (0.1898 versus 0.2419) in the DIOR dataset. Notably, both IRSDE and EDiffSR utilize the same diffusion process equation, i.e., SDE. Therefore, the results demonstrate the superiority of our EANet in providing effective noise prediction capabilities compared with the commonly employed UNet architecture in IRSDE. As for the DISTS metrics, we observe that despite SPSR focusing on preserving structural details, it only achieves the second-best performance on the DOTA and DIOR datasets. In contrast, our EDiffSR excels in attaining the best DISTS scores for both DOTA and DIOR, highlighting its remarkable capability to restore accurate structural details in RSIs. Moreover, EDiffSR can achieve the best NIQE values in almost all test sets. As a result, the proposed EDiffSR does recover realistic results that align well with human perception.

Besides the above results, the PSNR and SSIM results are also tabulated in Table III. The best and second-best performances within each category of methods are highlighted in bold and underlined. PSNR-oriented models, such as EDSR, RCAN, and HAT-L, achieve higher PSNR and SSIM scores

TABLE I  
QUANTITATIVE FID COMPARISON WITH SOTA SR MODELS ON 30 SCENE CATEGORIES OF THE AID TEST SET.  
THE BEST FID VALUE IN EACH CATEGORY IS HIGHLIGHTED IN RED, WHILE THE SECOND BEST IS IN BLUE

Categories	Bicubic	EDSR [2]	RCAN [3]	HAT-L [4]	MSRGAN [5]	ESRGAN [6]	SPSR [7]	SR3 [8]	IRSDE [9]	EDiffSR
Airport	126.23	87.25	89.52	86.55	54.42	54.85	57.98	56.56	<b>54.27</b>	<b>52.76</b>
Bare Land	113.49	91.50	92.51	91.15	66.83	<b>60.75</b>	72.17	76.89	80.30	<b>66.76</b>
Baseball Field	131.28	89.17	91.09	90.06	<b>51.25</b>	<b>46.87</b>	55.88	70.22	57.67	52.43
Beach	121.31	104.78	106.03	101.27	50.90	48.96	52.78	50.81	<b>43.22</b>	<b>43.10</b>
Bridge	137.67	80.01	82.27	80.93	<b>47.43</b>	50.70	49.40	73.65	<b>45.71</b>	50.98
Center	140.22	71.42	74.34	71.55	50.27	54.30	48.24	52.00	<b>44.29</b>	<b>43.13</b>
Church	122.26	85.76	87.92	89.48	51.88	51.89	55.03	62.58	<b>50.76</b>	<b>50.70</b>
Commercial	112.45	109.99	110.88	104.21	55.42	56.18	60.77	69.68	<b>51.84</b>	<b>55.20</b>
DenseResidential	126.36	113.85	125.26	118.28	52.16	57.75	55.99	62.96	<b>39.53</b>	<b>39.97</b>
Desert	115.10	77.50	76.95	75.84	56.28	<b>53.54</b>	64.02	59.35	61.50	<b>52.91</b>
Farmland	144.78	92.15	93.80	96.13	66.34	<b>56.12</b>	58.00	79.39	61.85	<b>51.07</b>
Forest	103.57	88.79	93.45	96.26	59.69	64.36	62.01	72.07	<b>48.68</b>	<b>46.90</b>
Industrial	106.82	77.84	80.85	74.83	37.79	<b>37.11</b>	45.90	46.07	<b>35.90</b>	41.27
Meadow	133.81	107.78	106.18	103.1	95.57	68.95	<b>64.83</b>	87.56	70.93	<b>66.53</b>
MediumResidential	117.19	98.74	104.17	100.24	46.17	50.11	49.75	73.45	<b>41.80</b>	<b>40.05</b>
Mountain	103.15	105.5	105.64	103.68	57.93	<b>54.93</b>	71.01	72.67	59.02	<b>52.21</b>
Park	137.79	109.64	112.28	109.54	<b>61.02</b>	<b>60.33</b>	72.14	80.81	63.78	63.29
Parking	134.86	60.79	67.40	63.98	41.79	42.99	45.40	56.09	<b>37.02</b>	<b>36.74</b>
Playground	113.86	58.07	61.90	60.36	40.69	39.15	41.00	53.96	<b>38.89</b>	<b>35.94</b>
Pond	162.50	122.29	124.27	126.31	60.65	<b>54.71</b>	62.62	104.36	56.29	<b>55.97</b>
Port	134.94	77.12	80.02	80.55	46.76	<b>46.72</b>	52.02	58.93	<b>46.52</b>	48.22
Railway Station	113.35	93.26	93.77	87.06	50.38	52.08	58.44	56.59	<b>49.82</b>	<b>51.89</b>
Resort	131.05	99.11	104.87	105.46	59.79	61.77	67.71	69.35	<b>59.00</b>	<b>57.26</b>
River	151.14	106.24	109.20	108.06	<b>54.50</b>	59.23	65.18	83.28	60.27	<b>57.34</b>
School	110.22	85.48	89.16	82.25	49.53	50.33	53.65	60.20	<b>47.60</b>	<b>47.00</b>
SparseResidential	149.02	134.24	140.41	132.73	73.57	75.55	77.83	85.06	<b>69.59</b>	<b>71.52</b>
Square	108.42	70.79	75.52	71.89	<b>42.48</b>	44.89	46.29	52.92	45.04	<b>42.43</b>
Stadium	121.79	56.48	59.39	58.87	37.70	35.28	37.42	38.27	<b>32.59</b>	<b>34.18</b>
Storage Tanks	161.44	89.80	93.90	88.43	45.57	51.67	51.01	53.38	<b>45.09</b>	<b>42.93</b>
Viaduct	109.83	66.8	68.89	66.65	36.11	34.32	37.66	46.14	<b>33.55</b>	<b>32.81</b>
Average	126.53	90.40	93.39	90.86	53.36	52.55	56.40	65.51	<b>51.08</b>	<b>49.45</b>

TABLE II  
QUANTITATIVE COMPARISON WITH SOTA SR MODELS IN TERMS OF FID, LPIPS, DISTs, AND NIQE ACROSS AID, DOTA,  
AND DIOR TEST SETS. THE BEST PERFORMANCE VALUE IS HIGHLIGHTED IN RED, WHILE THE SECOND BEST IS IN BLUE

Dataset	Metrics	Baseline			Regression-based			GAN-based			Diffusion-based	
		Bicubic	EDSR [2]	RCAN [3]	HAT-L [4]	MSRGAN [5]	ESRGAN [6]	SPSR [7]	SR3 [8]	IRSDE [9]	EDiffSR	
AID [60]	FID ↓	126.53	90.40	93.39	90.86	56.36	52.55	56.40	65.51	<b>51.08</b>	<b>49.45</b>	
	LPIPS ↓	0.4801	0.3068	0.3112	0.3078	<b>0.1694</b>	<b>0.1695</b>	0.1751	0.2534	0.2247	0.1887	
	DISTS ↓	0.1512	0.0880	0.0900	0.0882	0.0590	0.0601	0.0632	0.0903	<b>0.0579</b>	<b>0.0561</b>	
	NIQE ↓	21.24	19.79	19.88	20.15	17.46	15.51	17.90	15.16	<b>14.80</b>	<b>14.22</b>	
DOTA [2]	FID ↓	65.99	55.22	43.37	42.61	25.12	24.42	26.42	35.74	<b>23.91</b>	<b>21.26</b>	
	LPIPS ↓	0.4416	0.2616	0.2629	0.2641	0.1649	<b>0.1506</b>	<b>0.1605</b>	0.2790	0.1919	0.1689	
	DISTS ↓	0.1481	0.0831	0.0846	0.0832	0.0589	0.0582	0.0617	0.0993	<b>0.0550</b>	<b>0.0556</b>	
	NIQE ↓	19.48	18.37	18.58	18.98	16.71	15.48	18.01	15.49	<b>14.47</b>	<b>14.20</b>	
DIOR [62]	FID ↓	57.42	41.87	43.20	41.94	23.16	22.51	24.02	29.60	<b>22.28</b>	<b>21.79</b>	
	LPIPS ↓	0.4678	0.3020	0.3048	0.3062	<b>0.1722</b>	0.1836	<b>0.1772</b>	0.2836	0.2419	0.1898	
	DISTS ↓	0.1497	0.0886	0.0899	0.0893	<b>0.0605</b>	0.0623	0.0654	0.0924	0.0622	<b>0.0590</b>	
	NIQE ↓	20.24	19.16	19.30	19.56	17.61	<b>15.13</b>	18.24	15.55	15.19	<b>15.16</b>	

when compared with GAN-based and DPM-based SR methods. This is because they optimize MSE, which provides a straightforward learning objective for high PSNR performance. In particular, PSNR and SSIM are inconsistent with human perceptual while guiding the network to generate oversmooth content. As demonstrated in Table II, despite HAT-L achieving the highest PSNR score, it gains undesired scores in terms of FID, DISTs, and LPIPS. Furthermore, PSNR-driven methods tend to produce blurry results, resulting in poor perceptual quality. In the DPM-based category, our EDiffSR

consistently delivers higher quality results while maintaining the best PSNR/SSIM performance. When compared with SR3, we achieve a significant improvement in terms of PSNR (27.40 versus 26.24 dB) in the AID test set, demonstrating that our lightweight EANet is capable of providing excellent denoising performance in SR tasks.

2) *Qualitative Comparison:* We conducted a visual comparison with all comparative models. From Fig. 7, we find that our EDiffSR can consistently produce photorealistic results that surpass SOTA approaches. For the “center\_256” in AID,

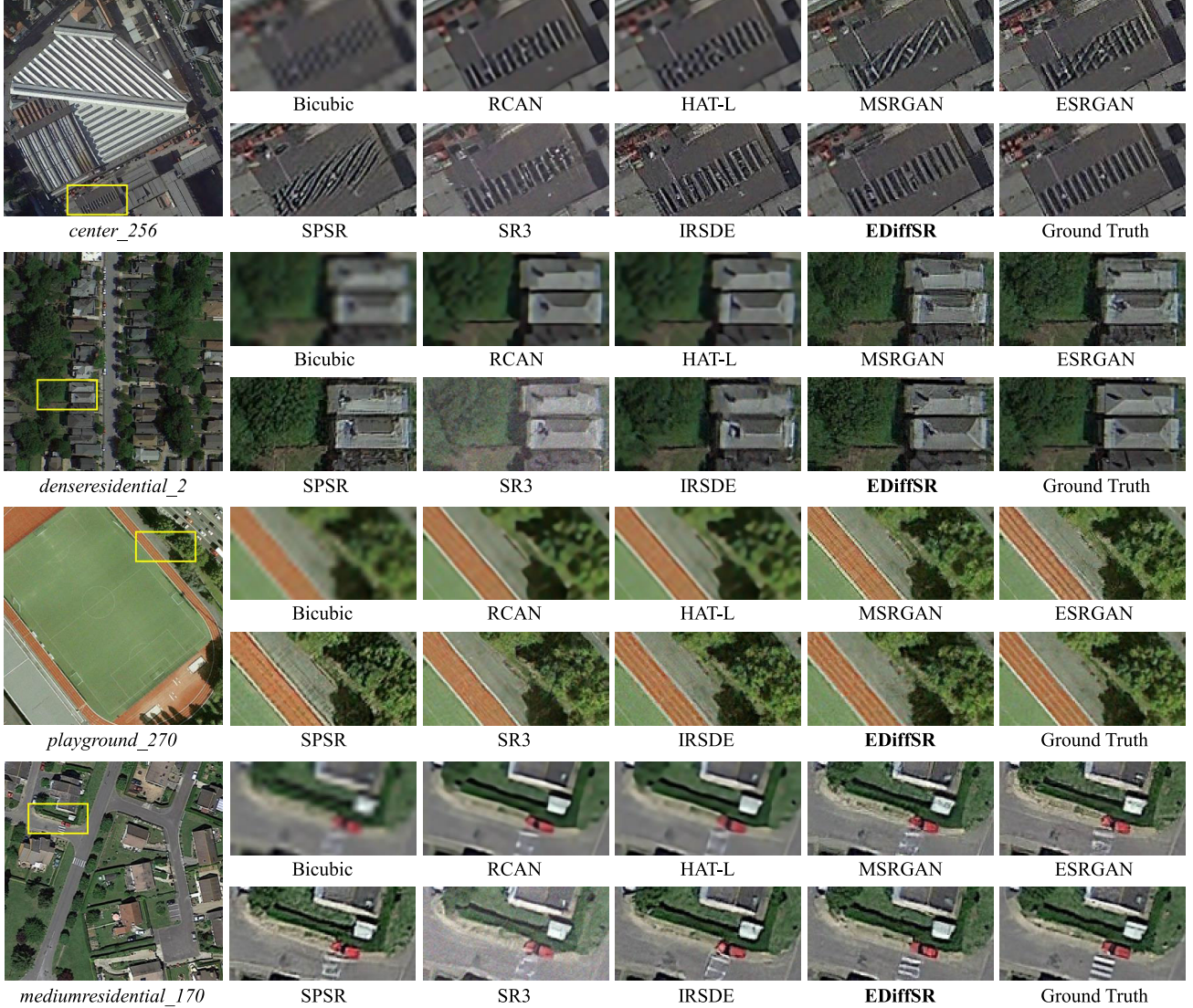


Fig. 7. 4 $\times$  visual comparisons with SOTA SR models on AID test set. The results show that our EDiffSR significantly outperforms comparative approaches in high-frequency detail recovery while producing visually pleasing images that are more natural. Zoomed-in view for a better view.

both RCAN and HAT-L produce blurry results, highlighting the limited generalization of PSNR-oriented models in recovering rich details. In contrast, GAN-based models can restore shape details, especially edge information, but often introduce severe artifacts inconsistent with the ground truth. EDiffSR consistently delivers more natural and realistic results, demonstrating its capacity to generate visually pleasing images. For the “mediumresidential\_170” image, RCAN and HAT-L still exhibit an oversmoothed appearance, while other GAN-based and diffusion-based models yield more natural results with realistic details. Compared with IRSDE and SR3, which directly adopt the bicubic interpolation to prepare conditions, EDiffSR contains more context details that are close to the ground-truth image, such as the marks on the road. The results demonstrate that the proposed CPEM is helpful in exploring more useful priors, e.g., edge information, thus boosting the performance of DPM in SR tasks.

In Fig. 8, we also visualize some SR results on the DOTA test set. As shown in Fig. 8, both regression-based

TABLE III  
QUANTITATIVE COMPARISON WITH SOTA SR MODELS IN TERMS OF PSNR, AND SSIM ACROSS AID, DOTA, AND DIOR TEST SETS. THE BEST PERFORMANCE VALUE IN EACH MODEL TYPE IS HIGHLIGHTED IN **BOLD**, WHILE THE SECOND BEST IS IN UNDERLINE

Method	AID [60]		DOTA [61]		DIOR [62]	
	PSNR	SSIM	PSNR	SSIM	PSNR	SSIM
EDSR [2]	30.65	0.8085	33.64	0.8648	30.63	0.8116
RCAN [3]	<b>30.82</b>	<u>0.8121</u>	<u>33.86</u>	<u>0.8680</u>	<u>30.85</u>	<u>0.8159</u>
HAT-L [4]	<u>30.81</u>	<b>0.8124</b>	<u>33.99</u>	<b>0.8684</b>	<u>30.87</u>	<b>0.8161</b>
MSRGAN [5]	<b>28.75</b>	<b>0.7390</b>	<b>29.46</b>	<b>0.7825</b>	<b>28.84</b>	<b>0.7422</b>
ESRGAN [6]	28.38	0.7272	29.01	0.7716	28.07	0.7086
SPSR [7]	27.71	0.7081	28.00	0.7696	27.46	0.7106
SR3 [8]	26.24	0.6705	27.62	0.6804	26.18	0.6639
IRSDE [9]	27.19	0.6585	28.08	0.7133	27.11	0.6516
EDiffSR (Ours)	<b>27.40</b>	<b>0.6805</b>	<b>28.30</b>	<b>0.7345</b>	<u>27.55</u>	<b>0.6823</b>

approaches and GAN-based models fail to achieve satisfactory detail, especially in terms of edges and textures. For

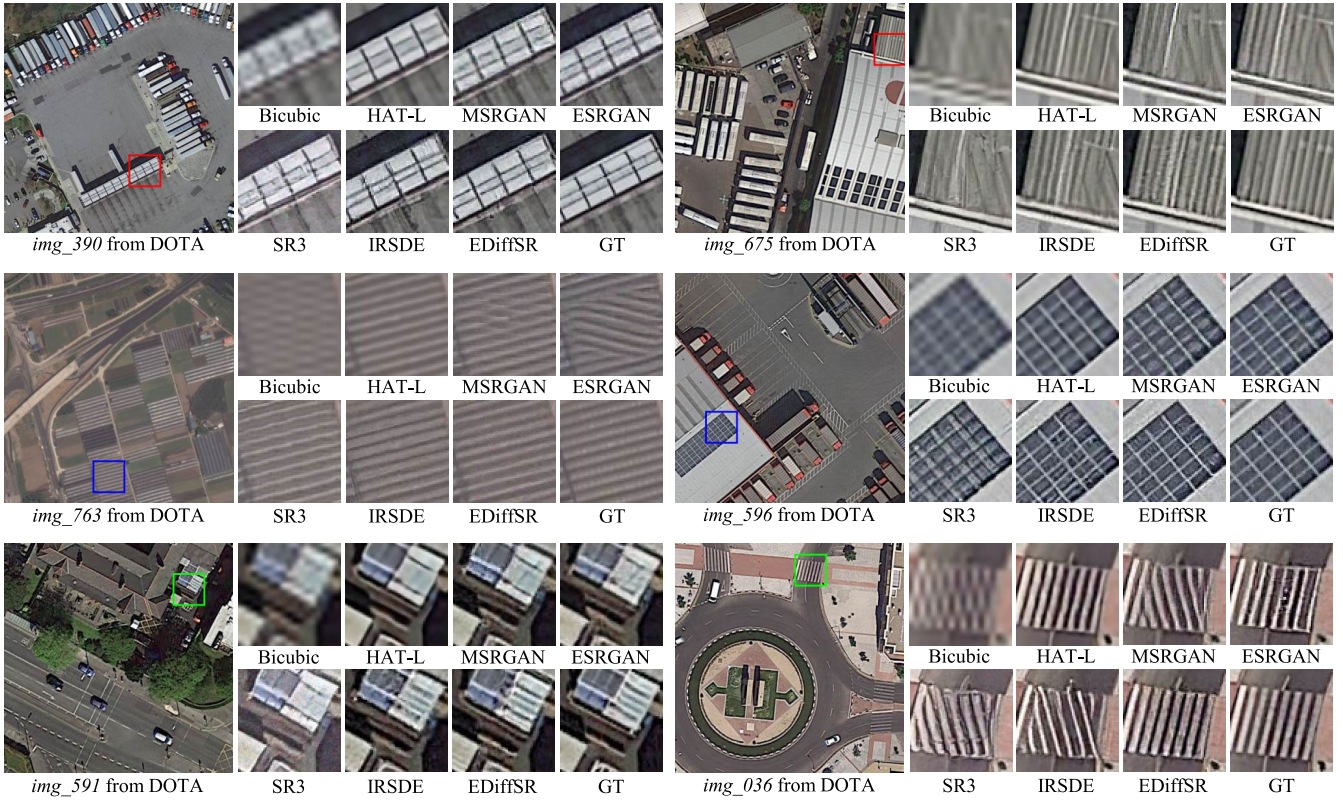


Fig. 8. 4 $\times$  visual comparisons with SOTA SR models on DOTA test set. Zoomed-in view for a better view.

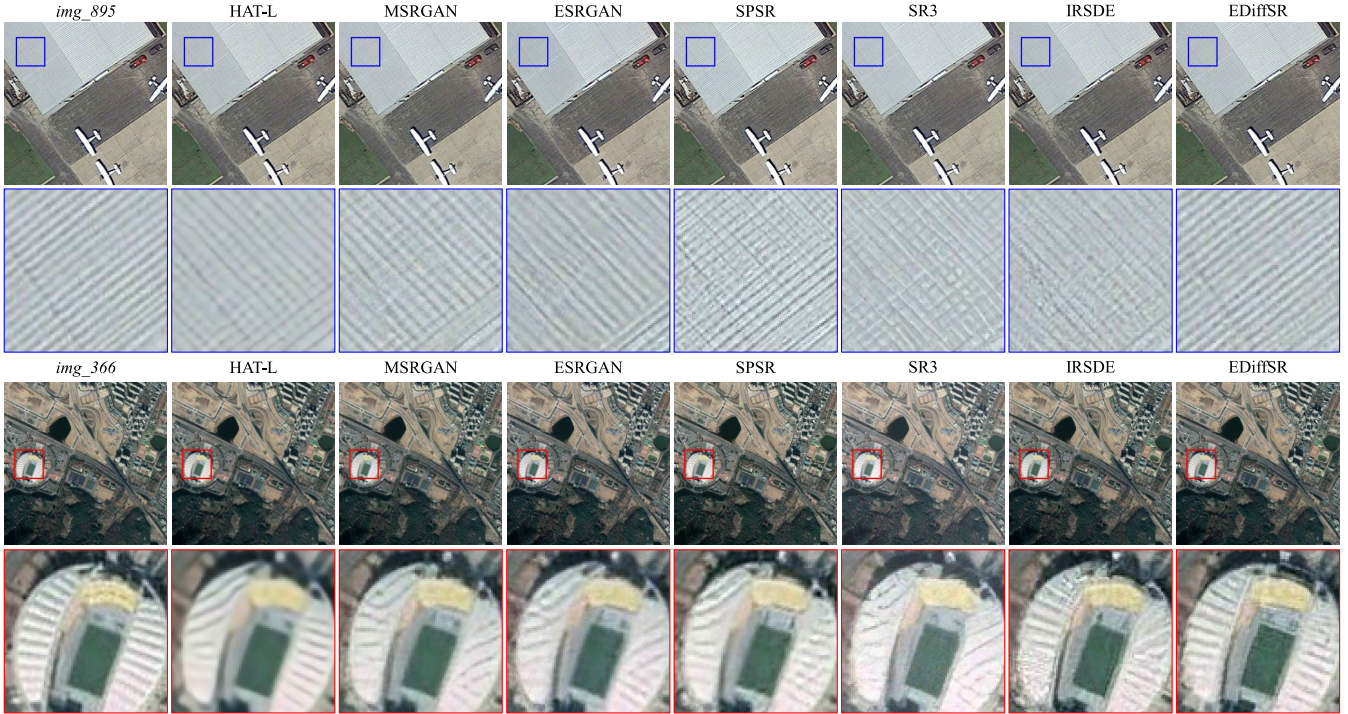


Fig. 9. 4 $\times$  visual comparisons with SOTA SR models on DIOR test set. Zoomed-in view for a better view.

“img\_591” from DOTA, only EDiffSR successfully restores the clear and sharp details of the building on the ground. In “img\_036”, MSRGAN, SR3, and IRSDE exhibit severe distortion, which deviates from the ground-truth distribution.

HAT-L and ESRGAN can offer relatively realistic distribution, restoring accurate direction of the lines on the road. Nevertheless, the results obtained from ESRGAN exhibit an unnatural appearance due to the oversharpening issue.

TABLE IV

QUANTITATIVE COMPARISON WITH SOTA SR MODELS IN TERMS OF NIQE, AND AG ON NWPU-RESISC45 TEST SET. THE BEST PERFORMANCE VALUE IS HIGHLIGHTED IN RED, WHILE THE SECOND BEST IN BLUE

Metrics	Bicubic	RCAN [3]	HAT-L [4]	MSRGAN [5]	ESRGAN [6]	SPSR [7]	SR3 [8]	IRSDE [9]	EDiffSR
NIQE ↓	20.8032	20.4722	20.3153	17.3114	17.9991	18.0730	17.8176	<b>16.5357</b>	<b>16.3013</b>
AG ↑	2.3556	3.0296	3.0081	3.3771	3.5170	3.5723	4.0101	<b>4.2690</b>	<b>4.7461</b>

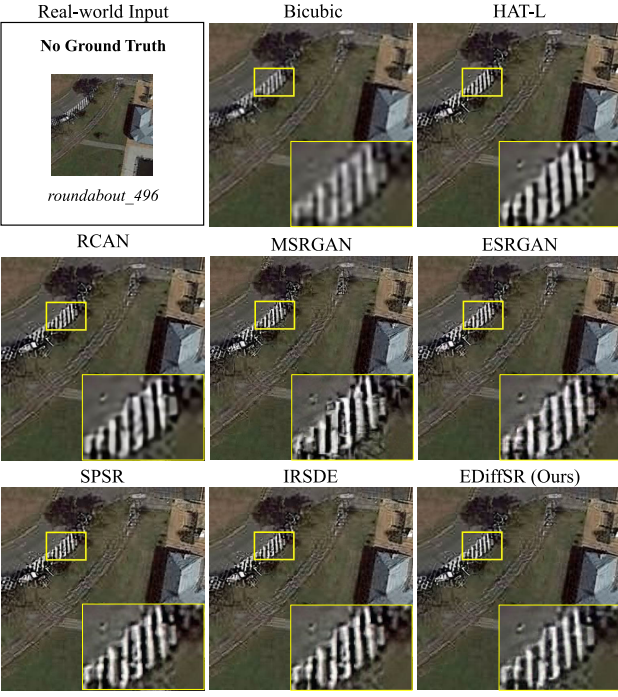


Fig. 10. 4× visual comparisons with SOTA SR models on NWPU-RESISC45 with real-world degradations. Zoomed-in view for a better view.

In contrast, EDiffSR accurately generates these details and appears more natural perception. These results highlight the capability of CPEM to explore additional prior information, enabling EDiffSR to recover more details that align with the realistic distribution of the ground truth.

In Fig. 9, we zoomed in and displayed some visual results from the DOIR dataset. As shown in “img\_895,” EDiffSR exhibits an impressive visual performance, outperforming other methods in accurately recovering the direction of the lines on the building roof. In this context, reconstructing such high-frequency information can be challenging. All methods yielded a completely wrong distribution of these details, except our EDiffSR. Benefiting from our condition prior enhancement module (CPEM), more high-frequency prior information can be explored and introduced into the diffusion process, making the output images consistent with the spatial distribution of ground-truth images. In “img\_366,” we zoomed in on the stadium region for comparison. It is evident that our EDiffSR reconstructs the most realistic results, whereas the other models exhibit significant distortion and blurring.

3) *Real-World Comparison:* We also evaluate the performance of our EDiffSR on real-world RSIs, i.e., without performing simulated degradations. Table IV shows the quantitative comparison of EDiffSR against SOTA methods in terms of NIQE and AG. We can see that EDiffSR achieves the best NIQE performance, illustrating our method can restore

TABLE V

ABLATION ANALYSIS OF EDIFFSR WITH DIFFERENT COMPONENTS. THE BEST FID, PSNR, AND NIQE PERFORMANCE IS SHOWN IN BOLD

Methods	$f_{CPREM}$	EANet	UNet	Param. (M)	FID↓	PSNR↑	NIQE↓
Baseline	✗	✗	✓	137.15	32.42	26.58	17.84
Model-1	✓	✗	✓	137.59	32.68	26.54	17.53
Model-2	✗	✓	✗	26.34	31.11	<b>27.81</b>	16.67
EDiffSR	✓	✓	✗	26.79	<b>30.83</b>	27.75	<b>16.30</b>

natural images that align with human perception in real-world scenarios. In addition, the best AG performance demonstrates that our reconstructed image contains more high-frequency detail information, such as edges and textures.

More intuitively, we display the visual comparison on the NWPU-RESISC45 dataset. The qualitative results are shown in Fig. 10. We can see that the PSNR-driven approach HAT-L exhibits a significantly blurry effect compared with the other approaches, whereas GAN-based methods, such as MSRGAN, produce excessively sharpened results accompanied by pseudo-details. In the diffusion-based methods, SR3 shows limitations in recovering precise edge information of the dense lines on the ground. In contrast, our method demonstrates the clearest preservation of high-frequency texture information, with minimal blurring and artifacts.

### E. Ablation Studies

In this section, we conduct extensive experiments to demonstrate the effectiveness of each component within our EDiffSR.

1) *Component Analysis of EDiffSR:* To investigate the holistic effectiveness of each part within EDiffSR, we remove the conditional prior enhancement ( $f_{CPREM}$ ), the EANet to form the three models reported in Table V. Note that once we remove the EANet, we replace it with the Vanilla UNet for noise prediction. By comparing Model-1 and EDiffSR, we can find that EANet is superior in improving the FID performance than UNet (30.83 versus 32.68) while reducing the model size by a large margin (26.31M versus 137.15M). After adding the  $f_{CPREM}$  in Model-2, we observe a slight parameter increase, but the improvement in FID is significant. When the whole  $f_{CPREM}$  and EANet are absent in baseline, the model performs poorly in FID. These results demonstrate that the proposed  $f_{CPREM}$  and EANet are able to improve the performance of the diffusion model. Besides, both  $f_{CPREM}$  and EANet have low complexity, allowing EDiffSR efficient yet effective.

2) *Effectiveness of EANet:* We first investigate the impact of varying channel numbers of EANet. As shown in Fig. 11, we find that EDiffSR achieves slightly superior FID performance when  $C = 128$  compared with  $C = 64$ . However, it was observed that EDiffSR yields the highest PSNR results when  $C = 64$ . To strike a favorable balance between model size and

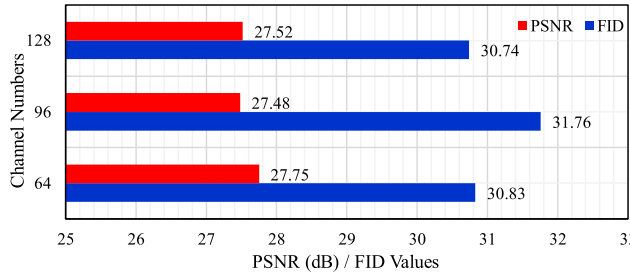
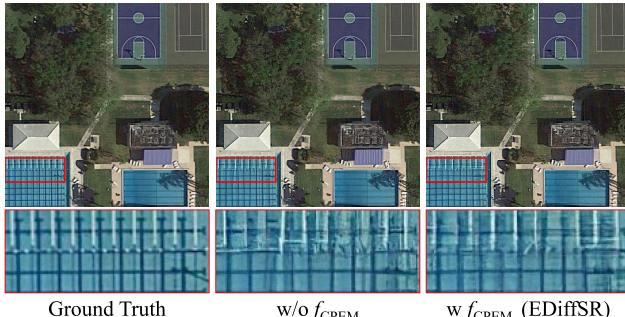
Fig. 11. Ablation analysis of EANet with different channel numbers  $C$ .Fig. 12. 4 $\times$  visual comparisons of the EDiffSR model without and with the CPEM  $f_{\text{CPEM}}$  on ‘img\_074’ from the DOTA test set. Image restored by the complete EDiffSR shows more high-frequency details than those recovered without  $f_{\text{CPEM}}$ .

TABLE VI

ABLATION ANALYSIS OF EANET WITH DIFFERENT SCALES OF CONVOLUTION.  $3 \times 3$ ,  $5 \times 5$ , AND  $7 \times 7$  REPRESENT SINGLE-SCALE DESIGN WITH DIFFERENT DWCONV KERNELS. EDIFFSR ADOPTS THE MULTISCALE DESIGN AND ACHIEVES MODEST IMPROVEMENT

Methods	$3 \times 3$	$5 \times 5$	$7 \times 7$	EDiffSR (Ours)
FID ↓	30.98	31.17	31.06	<b>30.83</b>
PSNR ↑	27.59	27.77	<b>27.89</b>	27.75

TABLE VII

MODEL EFFICIENCY ANALYSIS WITH SOTA SR MODELS.  
THE BEST PERFORMANCE IS SHOWN IN BOLD

Methods	Param. (M)	Running Time (s)	FID ↓	PSNR (dB) ↑
EDSR [2]	43.09	0.93	62.50	31.64
RCAN [3]	15.59	0.29	59.99	31.84
HAT-L [4]	40.32	0.76	58.47	<b>31.89</b>
MSRGAN [5]	<b>1.52</b>	<b>0.19</b>	34.88	29.02
ESRGAN [6]	16.70	0.22	33.16	28.49
SPSR [7]	24.79	0.60	35.61	27.72
SR3 [8]	92.56	137.61	43.61	26.68
IRSDE [9]	137.15	27.90	32.42	27.46
EDiffSR (Ours)	26.79	19.26	<b>30.83</b>	27.75

performance, we set  $C = 64$  in our final EDiffSR. Moreover, we conducted three experiments to assess the impact of multiscale design in EAB. The results are listed in Table VI. From the table, we can see that the multiscale design brings a modest improvement in terms of FID.

3) *Effectiveness of Conditional Prior Enhancement*: To further illustrate the capability of  $f_{\text{CPEM}}$  in grasping valuable prior knowledge for accurate SR reconstruction, we provide a visual comparison in Fig. 12. From this figure, we can see that the model with  $f_{\text{CPEM}}$  excels in recovering high-frequency details, such as edges and boundaries. This observation highlights that

$f_{\text{CPEM}}$  indeed boosts the performance of EDiffSR by exploring an enriched condition with more priors.

4) *Model Efficiency*: To demonstrate the efficiency of EDiffSR, we conducted a comparison of parameters and inference times, as presented in Table VII. The results indicate that EDiffSR is far more lightweight compared with the existing DPM-based SR models. For instance, when compared with IRSDE, EDiffSR achieves an impressive reduction of nearly 80% in model parameters (26.79M versus 137.15M) while delivering superior performance in both FID (30.83 versus 32.42) and PSNR (27.75 versus 27.46 dB). Furthermore, EDiffSR exhibits faster inference compared with the existing DPM-based models. When compared with SR3, EDiffSR is 7 $\times$  faster (19.26 versus 137.61 s) in the diffusion sampling process, making it more practical for real-world applications.

## VI. CONCLUSION

In this article, we devise an EDiffSR to generate perceptual-pleasant SR results of RSIs. The proposed EANet shows superior performance against vanilla UNet in noise prediction and is more lightweight. In particular, rather than employing the interpolated condition, a CPEM is designed to explore the potential priors from LR input, which significantly boosts the reconstruction performance. Extensive quantitative and qualitative evaluation on various remote-sensing datasets demonstrated that our EDiffSR outperforms SOTA regression-based, GAN-based, and diffusion-based SR methods.

Nevertheless, our EDiffSR does exhibit some shortcomings. First, the sampling process of the diffusion model consumes massive computational costs, which hinders its real-time application. Second, EDiffSR does not consider the multiple degradations involved in RSIs, resulting in limited adaptability to real-world scenes. Therefore, more efforts should be paid to speed up the sampling process of the diffusion model in the future direction. Moreover, we consider extending our EDiffSR to blind SR issues, thus improving its generalization in real-world scenarios.

## REFERENCES

- [1] M. Heusel, H. Ramsauer, T. Unterthiner, B. Nessler, and S. Hochreiter, “GANs trained by a two time-scale update rule converge to a local Nash equilibrium,” in *Proc. Adv. Neural Inf. Process. Syst.*, vol. 30, 2017, pp. 1–12.
- [2] B. Lim, S. Son, H. Kim, S. Nah, and K. M. Lee, “Enhanced deep residual networks for single image super-resolution,” in *Proc. IEEE Conf. Comput. Vis. Pattern Recognit. Workshops (CVPRW)*, Jul. 2017, pp. 1132–1140.
- [3] Y. Zhang, K. Li, K. Li, L. Wang, B. Zhong, and Y. Fu, “Image super-resolution using very deep residual channel attention networks,” in *Proc. Eur. Conf. Comput. Vis. (ECCV)*, 2018, pp. 286–301.
- [4] X. Chen, X. Wang, J. Zhou, Y. Qiao, and C. Dong, “Activating more pixels in image super-resolution transformer,” in *Proc. IEEE/CVF Conf. Comput. Vis. Pattern Recognit. (CVPR)*, Jun. 2023, pp. 22367–22377.
- [5] C. Ledig et al., “Photo-realistic single image super-resolution using a generative adversarial network,” in *Proc. IEEE Conf. Comput. Vis. Pattern Recognit. (CVPR)*, Jul. 2017, pp. 105–114.
- [6] X. Wang et al., “ESRGAN: Enhanced super-resolution generative adversarial networks,” in *Proc. Eur. Conf. Comput. Vis. (ECCV) Workshops*, 2018, pp. 1–17.
- [7] C. Ma, Y. Rao, J. Lu, and J. Zhou, “Structure-preserving image super-resolution,” *IEEE Trans. Pattern Anal. Mach. Intell.*, vol. 44, no. 11, pp. 7898–7911, Nov. 2022.

- [8] C. Saharia, J. Ho, W. Chan, T. Salimans, D. J. Fleet, and M. Norouzi, “Image super-resolution via iterative refinement,” *IEEE Trans. Pattern Anal. Mach. Intell.*, vol. 45, no. 4, pp. 4713–4726, Apr. 2023.
- [9] Z. Luo, F. K. Gustafsson, Z. Zhao, J. Sjolund, and T. B. Schon, “Image restoration with mean-reverting stochastic differential equations,” in *Proc. Int. Conf. Mach. Learn.*, 2023, pp. 1–25.
- [10] J. He et al., “Spectral super-resolution meets deep learning: Achievements and challenges,” *Inf. Fusion*, vol. 97, Sep. 2023, Art. no. 101812.
- [11] Y. Xiao, Q. Yuan, Q. Zhang, and L. Zhang, “Deep blind super-resolution for satellite video,” *IEEE Trans. Geosci. Remote Sens.*, vol. 61, 2023, pp. 1–16, Art. no. 5516316.
- [12] D. Liu et al., “An efficient unfolding network with disentangled spatial-spectral representation for hyperspectral image super-resolution,” *Inf. Fusion*, vol. 94, pp. 92–111, Jun. 2023.
- [13] R. Dian, A. Guo, and S. Li, “Zero-shot hyperspectral sharpening,” *IEEE Trans. Pattern Anal. Mach. Intell.*, vol. 45, no. 10, pp. 12650–12666, Oct. 2023.
- [14] D. He and Y. Zhong, “Deep hierarchical pyramid network with high-frequency-aware differential architecture for super-resolution mapping,” *IEEE Trans. Geosci. Remote Sens.*, vol. 61, 2023, pp. 1–15, Art. no. 5503815.
- [15] D. He, Q. Shi, X. Liu, Y. Zhong, G. Xia, and L. Zhang, “Generating annual high resolution land cover products for 28 metropolises in China based on a deep super-resolution mapping network using Landsat imagery,” *GIScience Remote Sens.*, vol. 59, no. 1, pp. 2036–2067, Dec. 2022.
- [16] J. Wang, A. Ma, Y. Zhong, Z. Zheng, and L. Zhang, “Cross-sensor domain adaptation for high spatial resolution urban land-cover mapping: From airborne to spaceborne imagery,” *Remote Sens. Environ.*, vol. 277, Aug. 2022, Art. no. 113058.
- [17] J. He, Q. Yuan, J. Li, Y. Xiao, and L. Zhang, “A self-supervised remote sensing image fusion framework with dual-stage self-learning and spectral super-resolution injection,” *ISPRS J. Photogramm. Remote Sens.*, vol. 204, pp. 131–144, Oct. 2023.
- [18] R. Dian, S. Li, and X. Kang, “Regularizing hyperspectral and multispectral image fusion by CNN denoiser,” *IEEE Trans. Neural Netw. Learn. Syst.*, vol. 32, no. 3, pp. 1124–1135, Mar. 2021.
- [19] Y. Xiao, Y. Wang, Q. Yuan, J. He, and L. Zhang, “Generating a long-term (2003–2020) hourly 0.25° global PM<sub>2.5</sub> dataset via spatiotemporal downscaling of CAMS with deep learning (DeepCAMS),” *Sci. Total Environ.*, vol. 848, Nov. 2022, Art. no. 157747.
- [20] Y. Xiao et al., “Space-time super-resolution for satellite video: A joint framework based on multi-scale spatial-temporal transformer,” *Int. J. Appl. Earth Observ. Geoinf.*, vol. 108, Apr. 2022, Art. no. 102731.
- [21] Q. Zhang, Y. Zheng, Q. Yuan, M. Song, H. Yu, and Y. Xiao, “Hyperspectral image denoising: From model-driven, data-driven, to model-data-driven,” *IEEE Trans. Neural Netw. Learn. Syst.*, early access, pp. 1–21, Jun. 2023, doi: [10.1109/TNNLS.2023.3278866](https://doi.org/10.1109/TNNLS.2023.3278866).
- [22] Y.-C. Miao, X.-L. Zhao, X. Fu, J.-L. Wang, and Y.-B. Zheng, “Hyperspectral denoising using unsupervised disentangled spatiotemporal deep priors,” *IEEE Trans. Geosci. Remote Sens.*, vol. 60, 2022, pp. 1–16, Art. no. 5513916.
- [23] J. Zhou et al., “UGIF-Net: An efficient fully guided information flow network for underwater image enhancement,” *IEEE Trans. Geosci. Remote Sens.*, vol. 61, 2023, pp. 1–17, Art. no. 4206117.
- [24] J. Zhou, Q. Liu, Q. Jiang, W. Ren, K.-M. Lam, and W. Zhang, “Underwater camera: Improving visual perception via adaptive dark pixel prior and color correction,” *Int. J. Comput. Vis.*, early access, pp. 1–19, Aug. 2023, doi: [10.1007/s11263-023-01853-3](https://doi.org/10.1007/s11263-023-01853-3).
- [25] Q. Zhang, Q. Yuan, M. Song, H. Yu, and L. Zhang, “Cooperated spectral low-rankness prior and deep spatial prior for HSI unsupervised denoising,” *IEEE Trans. Image Process.*, vol. 31, pp. 6356–6368, 2022.
- [26] K. Jiang, Z. Wang, P. Yi, and J. Jiang, “Hierarchical dense recursive network for image super-resolution,” *Pattern Recognit.*, vol. 107, Nov. 2020, Art. no. 107475.
- [27] Y. Zhang, Y. Tian, Y. Kong, B. Zhong, and Y. Fu, “Residual dense network for image super-resolution,” in *Proc. IEEE/CVF Conf. Comput. Vis. Pattern Recognit.*, Jun. 2018, pp. 2472–2481.
- [28] J. Kim, J. K. Lee, and K. M. Lee, “Accurate image super-resolution using very deep convolutional networks,” in *Proc. IEEE Conf. Comput. Vis. Pattern Recognit. (CVPR)*, Jun. 2016, pp. 1646–1654.
- [29] Y. Mei, Y. Fan, and Y. Zhou, “Image super-resolution with non-local sparse attention,” in *Proc. IEEE/CVF Conf. Comput. Vis. Pattern Recognit. (CVPR)*, Jun. 2021, pp. 3516–3525.
- [30] J. He, Q. Yuan, J. Li, Y. Xiao, X. Liu, and Y. Zou, “DsTer: A dense spectral transformer for remote sensing spectral super-resolution,” *Int. J. Appl. Earth Observ. Geoinf.*, vol. 109, May 2022, Art. no. 102773.
- [31] J. Ho, A. Jain, and P. Abbeel, “Denoising diffusion probabilistic models,” in *Proc. Adv. Neural Inf. Process. Syst.*, vol. 33, 2020, pp. 6840–6851.
- [32] H. Li et al., “SRDiff: Single image super-resolution with diffusion probabilistic models,” *Neurocomputing*, vol. 479, pp. 47–59, Mar. 2022.
- [33] H. Wu, N. Ni, S. Wang, and L. Zhang, “Conditional stochastic normalizing flows for blind super-resolution of remote sensing images,” *IEEE Trans. Geosci. Remote Sens.*, vol. 61, 2023, pp. 1–16, Art. no. 5617916.
- [34] Y. Miao, L. Zhang, L. Zhang, and D. Tao, “DDS2M: Self-supervised denoising diffusion spatio-spectral model for hyperspectral image restoration,” in *Proc. IEEE/CVF Int. Conf. Comput. Vis.*, 2023, pp. 12086–12096.
- [35] C. Dong, C. C. Loy, K. He, and X. Tang, “Image super-resolution using deep convolutional networks,” *IEEE Trans. Pattern Anal. Mach. Intell.*, vol. 38, no. 2, pp. 295–307, Feb. 2016.
- [36] K. Simonyan and A. Zisserman, “Very deep convolutional networks for large-scale image recognition,” 2014, *arXiv:1409.1556*.
- [37] M. S. M. Sajjadi, B. Scholkopf, and M. Hirsch, “EnhanceNet: Single image super-resolution through automated texture synthesis,” in *Proc. IEEE Int. Conf. Comput. Vis. (ICCV)*, Oct. 2017, pp. 4491–4500.
- [38] R. Rombach, A. Blattmann, D. Lorenz, P. Esser, and B. Ommer, “High-resolution image synthesis with latent diffusion models,” in *Proc. IEEE/CVF Conf. Comput. Vis. Pattern Recognit. (CVPR)*, Jun. 2022, pp. 10674–10685.
- [39] B. Xia et al., “DiffIR: Efficient diffusion model for image restoration,” 2023, *arXiv:2303.09472*.
- [40] K. Jiang, Z. Wang, P. Yi, J. Jiang, J. Xiao, and Y. Yao, “Deep distillation recursive network for remote sensing imagery super-resolution,” *Remote Sens.*, vol. 10, no. 11, p. 1700, Oct. 2018.
- [41] S. Lei, Z. Shi, and W. Mo, “Transformer-based multistage enhancement for remote sensing image super-resolution,” *IEEE Trans. Geosci. Remote Sens.*, vol. 60, 2022, pp. 1–11, Art. no. 5615611.
- [42] Y. Xiao, Q. Yuan, K. Jiang, J. He, Y. Wang, and L. Zhang, “From degrade to upgrade: Learning a self-supervised degradation guided adaptive network for blind remote sensing image super-resolution,” *Inf. Fusion*, vol. 96, pp. 297–311, Aug. 2023.
- [43] Y. Xiao, X. Su, Q. Yuan, D. Liu, H. Shen, and L. Zhang, “Satellite video super-resolution via multiscale deformable convolution alignment and temporal grouping projection,” *IEEE Trans. Geosci. Remote Sens.*, vol. 60, 2022, pp. 1–19, Art. no. 5610819.
- [44] S. Lei and Z. Shi, “Hybrid-scale self-similarity exploitation for remote sensing image super-resolution,” *IEEE Trans. Geosci. Remote Sens.*, vol. 60, 2022, pp. 1–10, Art. no. 5401410.
- [45] S. Chen, L. Zhang, and L. Zhang, “MSDformer: Multiscale deformable transformer for hyperspectral image super-resolution,” *IEEE Trans. Geosci. Remote Sens.*, vol. 61, 2023, pp. 1–14, Art. no. 5525614.
- [46] D. Zhang, J. Shao, X. Li, and H. T. Shen, “Remote sensing image super-resolution via mixed high-order attention network,” *IEEE Trans. Geosci. Remote Sens.*, vol. 59, no. 6, pp. 5183–5196, Jun. 2021.
- [47] Y. Xiao et al., “Local-global temporal difference learning for satellite video super-resolution,” *IEEE Trans. Circuits Syst. Video Technol.*, early access, pp. 1–14, Sep. 2023, doi: [10.1109/TCSVT.2023.3312321](https://doi.org/10.1109/TCSVT.2023.3312321).
- [48] Q. Li, M. Gong, Y. Yuan, and Q. Wang, “Symmetrical feature propagation network for hyperspectral image super-resolution,” *IEEE Trans. Geosci. Remote Sens.*, vol. 60, 2022, pp. 1–12, Art. no. 5536912.
- [49] Q. Li, Y. Yuan, X. Jia, and Q. Wang, “Dual-stage approach toward hyperspectral image super-resolution,” *IEEE Trans. Image Process.*, vol. 31, pp. 7252–7263, 2022.
- [50] Q. Li, M. Gong, Y. Yuan, and Q. Wang, “RGB-induced feature modulation network for hyperspectral image super-resolution,” *IEEE Trans. Geosci. Remote Sens.*, vol. 61, 2023.
- [51] S. Lei, Z. Shi, and Z. Zou, “Coupled adversarial training for remote sensing image super-resolution,” *IEEE Trans. Geosci. Remote Sens.*, vol. 58, no. 5, pp. 3633–3643, May 2020.
- [52] K. Jiang, Z. Wang, P. Yi, G. Wang, T. Lu, and J. Jiang, “Edge-enhanced GAN for remote sensing image superresolution,” *IEEE Trans. Geosci. Remote Sens.*, vol. 57, no. 8, pp. 5799–5812, Aug. 2019.
- [53] J. M. Haut, R. Fernandez-Beltran, M. E. Paoletti, J. Plaza, A. Plaza, and F. Pla, “A new deep generative network for unsupervised remote sensing single-image super-resolution,” *IEEE Trans. Geosci. Remote Sens.*, vol. 56, no. 11, pp. 6792–6810, Nov. 2018.
- [54] J. Tu, G. Mei, Z. Ma, and F. Piccialli, “SWCGAN: Generative adversarial network combining Swin transformer and CNN for remote sensing image super-resolution,” *IEEE J. Sel. Topics Appl. Earth Observ. Remote Sens.*, vol. 15, pp. 5662–5673, 2022.

- [55] Z. Liu et al., "Swin transformer: Hierarchical vision transformer using shifted windows," in *Proc. IEEE/CVF Int. Conf. Comput. Vis. (ICCV)*, Oct. 2021, pp. 9992–10002.
- [56] J. Liu, Z. Yuan, Z. Pan, Y. Fu, L. Liu, and B. Lu, "Diffusion model with detail complement for super-resolution of remote sensing," *Remote Sens.*, vol. 14, no. 19, p. 4834, Sep. 2022.
- [57] W. Shi et al., "Real-time single image and video super-resolution using an efficient sub-pixel convolutional neural network," in *Proc. IEEE Conf. Comput. Vis. Pattern Recognit. (CVPR)*, Jun. 2016, pp. 1874–1883.
- [58] P. E. Kloeden, E. Platen, P. E. Kloeden, and E. Platen, *Stochastic Differential Equations*. Berlin, Germany: Springer, 1992.
- [59] G.-S. Xia et al., "AID: A benchmark data set for performance evaluation of aerial scene classification," *IEEE Trans. Geosci. Remote Sens.*, vol. 55, no. 7, pp. 3965–3981, Jul. 2017.
- [60] G.-S. Xia et al., "DOTA: A large-scale dataset for object detection in aerial images," in *Proc. IEEE/CVF Conf. Comput. Vis. Pattern Recognit.*, Jun. 2018, pp. 3974–3983.
- [61] K. Li, G. Wan, G. Cheng, L. Meng, and J. Han, "Object detection in optical remote sensing images: A survey and a new benchmark," *ISPRS J. Photogramm. Remote Sens.*, vol. 159, pp. 296–307, Jan. 2020.
- [62] G. Cheng, J. Han, and X. Lu, "Remote sensing image scene classification: Benchmark and state of the art," *Proc. IEEE*, vol. 105, no. 10, pp. 1865–1883, Oct. 2017.
- [63] R. Zhang, P. Isola, A. A. Efros, E. Shechtman, and O. Wang, "The unreasonable effectiveness of deep features as a perceptual metric," in *Proc. IEEE/CVF Conf. Comput. Vis. Pattern Recognit.*, Jun. 2018, pp. 586–595.
- [64] K. Ding, K. Ma, S. Wang, and E. P. Simoncelli, "Image quality assessment: Unifying structure and texture similarity," *IEEE Trans. Pattern Anal. Mach. Intell.*, vol. 44, no. 5, pp. 2567–2581, May 2022.
- [65] Z. Wang, A. C. Bovik, H. R. Sheikh, and E. P. Simoncelli, "Image quality assessment: From error visibility to structural similarity," *IEEE Trans. Image Process.*, vol. 13, no. 4, pp. 600–612, Apr. 2004.
- [66] T. Salimans et al., "Improved techniques for training GANs," in *Proc. Adv. Neural Inf. Process. Syst.*, vol. 29, 2016, pp. 1–9.
- [67] A. Mittal, R. Soundararajan, and A. C. Bovik, "Making a," completely blind image quality analyzer," *IEEE Signal Process. Lett.*, vol. 20, no. 3, pp. 209–212, Mar. 2012.



**Yi Xiao** received the B.S. degree from the School of Mathematics and Physics, China University of Geosciences, Wuhan, China, in 2020. He is currently pursuing the Ph.D. degree with the School of Geodesy and Geomatics, Wuhan University, Wuhan.

His major research interests are remote sensing image/video processing and computer vision.



**Qiangqiang Yuan** (Member, IEEE) received the B.S. degree in surveying and mapping engineering and the Ph.D. degree in photogrammetry and remote sensing from Wuhan University, Wuhan, China, in 2006 and 2012, respectively.

In 2012, he joined the School of Geodesy and Geomatics, Wuhan University, where he is currently a Professor. He has published more than 90 research papers, including more than 70 peer-reviewed articles in international journals, such as *Remote Sensing of Environment*, *ISPRS Journal of Photogrammetry and Remote Sensing*, *IEEE TRANSACTIONS ON IMAGE PROCESSING*, and *IEEE TRANSACTIONS ON GEOSCIENCE AND REMOTE SENSING*. His research interests include image reconstruction, remote sensing image processing and application, and data fusion.

Dr. Yuan was a recipient of the Youth Talent Support Program of China in 2019, the Top-Ten Academic Star of Wuhan University in 2011, and the recognition of Best Reviewers of the IEEE GRSL in 2019. In 2014, he received the Hong Kong Scholar Award from the Society of Hong Kong Scholars and the China National Postdoctoral Council. He is an associate editor of five international journals and has frequently served as a referee for more than 40 international journals for remote sensing and image processing.



**Kui Jiang** (Member, IEEE) received the Ph.D. degree from the School of Computer Science, Wuhan University, Wuhan, China, in 2022.

He is currently an Associate Professor with the School of Computer Science and Technology, Harbin Institute of Technology, Harbin, China. His research interests include image/video processing and computer vision.

Dr. Jiang received the 2022 ACM Wuhan Doctoral Dissertation Award.



**Jiang He** (Graduate Student Member, IEEE) received the B.S. degree in remote sensing science and technology from the Faculty of Geosciences and Environmental Engineering, Southwest Jiaotong University, Chengdu, China, in 2018. He is currently pursuing the Ph.D. degree with the School of Geodesy and Geomatics, Wuhan University, Wuhan, China.

His research interests include hyperspectral super-resolution, image fusion, quality improvement, remote sensing image processing, and deep learning.



**Xianyu Jin** received the B.S. degree in geodesy and geomatics engineering from Wuhan University, Wuhan, China, in 2019, where he is currently pursuing the M.S. degree with the School of Geodesy and Geomatics.

His research interests include video super-resolution, deep learning, and computer vision.



**Liangpei Zhang** (Fellow, IEEE) received the B.S. degree in physics from Hunan Normal University, Changsha, China, in 1982, the M.S. degree in optics from the Xi'an Institute of Optics and Precision Mechanics, Chinese Academy of Sciences, Xi'an, China, in 1988, and the Ph.D. degree in photogrammetry and remote sensing from Wuhan University, Wuhan, China, in 1998.

He was a Principal Scientist for the China State Key Basic Research Project from 2011 to 2016 and was appointed by the Ministry of National

Science and Technology of China to lead the Remote Sensing Program in China. He is currently a "Chang-Jiang Scholar" Chair Professor appointed by the Ministry of Education of China at the State Key Laboratory of Information Engineering in Surveying, Mapping, and Remote Sensing (LIESMARS), Wuhan University. He has published more than 700 research articles and five books. He is an Institute for Scientific Information (ISI) Highly Cited Author. He holds 30 patents. His research interests include hyperspectral remote sensing, high-resolution remote sensing, image processing, and artificial intelligence.

Dr. Zhang is a fellow of the Institution of Engineering and Technology (IET). He was a recipient of the 2010 Best Paper Boeing Award, the 2013 Best Paper ERDAS Award from the American Society of Photogrammetry and Remote Sensing (ASPRS), and the 2016 Best Paper Theoretical Innovation Award from the International Society for Optics and Photonics (SPIE). His research teams won the top three prizes of the IEEE GRSS 2014 Data Fusion Contest. His students have been selected as the winners or finalists of the IEEE International Geoscience and Remote Sensing Symposium (IGARSS) Student Paper Contest in recent years. He is also the Founding Chair of the IEEE Geoscience and Remote Sensing Society (GRSS) Wuhan Chapter. He also serves as an associate editor or an editor for more than ten international journals. He is also serving as an Associate Editor for IEEE TRANSACTIONS ON GEOSCIENCE AND REMOTE SENSING.